Research

Author for correspondence:

Luke G. Bennetts

e-mail: luke.bennetts@adelaide.edu.au

Tracking Rayleigh–Bloch waves swapping between Riemann sheets

Kei Matsushima[1], Luke G. Bennetts[2] and Malte A. Peter[3,4]

[1]Graduate School of Engineering, University of Tokyo, Tokyo 113–8656, Japan
[2]School of Computer and Mathematical Sciences, University of Adelaide, Adelaide, SA 5005, Australia
[3]Institute of Mathematics, University of Augsburg, Augsburg 86135, Germany
[4]Centre for Advanced Analytics and Predictive Sciences, University of Augsburg, Augsburg 86135, Germany

KM, 0000-0002-0352-8770; LGB, 0000-0001-9386-7882; MAP, 0000-0001-6107-9806

Rayleigh–Bloch waves are modes localized to periodic arrays of scatterers with unbounded unit cells. Here, Rayleigh–Bloch waves are studied for line arrays of sound-hard circular scatterers embedded in a two-dimensional acoustic medium, for which it has recently been shown that Rayleigh–Bloch waves exist for higher frequencies than previously thought. Moreover, it was shown that Rayleigh–Bloch waves can cut off (disappear) and cut on (reappear), and additional Rayleigh–Bloch waves can cut on and interact with the existing ones. These complicated behaviours are reconsidered using a family of quasi-periodic Green's functions that allow particular plane-wave components to become unbounded away from the array. The Green's function formulation is combined with the block Sakurai–Sugiura method to trace the trajectories of the Rayleigh–Bloch wavenumbers as they swap between Riemann sheets that are categorized according to the unbounded plane wave(s). A detailed analysis is presented for three different scatterer radius values, and contrasting qualitative behaviours are identified. The findings are consistent with those published previously, extend to higher frequencies than allowed by the previous approach, and provide new understanding of Rayleigh–Bloch waves around the critical frequency intervals where they cut on/cut off/interact.

THE ROYAL SOCIETY
PUBLISHING

1. Introduction

Rayleigh–Bloch waves are a class of Bloch mode supported by periodic arrays in which the unit cells are unbounded (the array dimension is less than the background medium), which decay towards the far-field and are, thus, localized to the arrays. They have been most often studied for diffraction gratings, i.e. one-dimensional (straight-line) arrays embedded in a two-dimensional background medium (figure 1) [1]. They are classically considered to propagate along the array without decay (in the x_1-direction; figure 1) and decay exponentially away from it (in the x_2-direction) [2]. They exist for sound-hard scatterers in acoustics [3] and the mathematically equivalent problem of arrays of vertical cylinders in a water domain with a free surface [2,4] as well as along thin plates [5,6]. In electromagnetics, they are known as array-guided surface waves or bound waves, and we refer to [5,7] for further discussion and references. For the past two to three decades, Rayleigh–Bloch waves have been an object of sustained research interest as they are known to have a large influence on the response of the corresponding semi-infinite or finite structures with equally spaced bodies [4,8–13].

The periodicity cell for Rayleigh–Bloch waves on diffraction gratings is unbounded in one direction (the x_2-direction) and Bloch (quasi-periodicity) conditions only apply at the opposing cell boundaries (in the x_1-direction). The Bloch conditions imply that the solution changes by a factor $\exp\{i\beta\}$ across the periodicity cell (from left to right), where $\beta(k)$ is the spectral parameter (eigenvalue) for a given frequency (or background wavenumber) k. (Note that the spacing along the grating has been normalized to unity; see figure 1.) Therefore, classical Rayleigh–Bloch waves can be interpreted as the limit of Bloch waves, in which a rectangular periodicity cell becomes infinitely long in the x_2-direction [14,15]. Because of the unbounded periodicity cell, the spectral structure is much richer than for the corresponding Bloch problem (in which the periodicity cell is bounded). In particular, a continuous spectrum of the corresponding eigenvalue problem is present, $\sigma_{cts}(k)$, containing β for which solutions exist to the eigenvalue problem that are bounded away from the array but do not decay. The eigenvalues for which these solutions exist are simply $\beta = k \cos \psi$, where $\psi \in [-\pi, \pi)$ can be interpreted as an incident wave direction, plus complex branches that generalize the incident waves [11]. There is also a point spectrum, $\sigma_{pt}(k)$, which contains eigenvalues, β, corresponding to solutions that decay away from the array, i.e. the solutions are Rayleigh–Bloch waves and the eigenvalues are referred to as Rayleigh–Bloch wavenumbers [2,11]. Note that some authors consider the spectrum in terms of frequency, i.e. they take the perspective of $k(\beta)$ rather than $\beta(k)$, e.g. [2].

Classical Rayleigh–Bloch waves have $\beta \in \mathbb{R}$, and noting (i) the above definition of the continuous spectrum and (ii) the eigenvalue problem is unchanged if multiples of 2π are added to β, the search for Rayleigh–Bloch wavenumbers can be reduced to the interval $k < \beta \leq \pi$. If β exists in this interval then it corresponds to a rightwards travelling Rayleigh–Bloch wave, and there is necessarily a leftwards travelling Rayleigh–Bloch wave with wavenumber $2\pi - \beta$. As frequency is increased, the continuous spectrum eventually covers the whole real line and the interval over which classical Rayleigh–Bloch wavenumbers can be found vanishes (when $k \geq \pi$). Just before this happens, the classical Rayleigh–Bloch waves 'cut off'. At the cut-off frequency, the wavenumbers of the rightwards and leftwards Rayleigh–Bloch waves meet at $\beta = \pi$, which gives a solution known as the Neumann trapped mode, as this corresponds to the case that the Bloch conditions at the boundary of the periodicity cell (or the channel walls) become homogeneous Neumann conditions. In the grating context, this corresponds to a standing wave, which is antisymmetric across the cell width. Classical Rayleigh–Bloch waves ($\beta \in \mathbb{R}$) have been shown to exist above the Neumann trapped mode frequency for isolated frequencies, which corresponds to eigenvalues embedded in the continuous spectrum [16]. The embedded eigenvalues can include $\beta = 2\pi$ (or, equivalently, $\beta = 0$), which is symmetric across the cell width and known as the Dirichlet trapped mode [8].

For a grating of sound-hard circular cylinders, a transfer operator approach has been used to show that the notion of Rayleigh–Bloch waves can be generalized beyond the Neumann
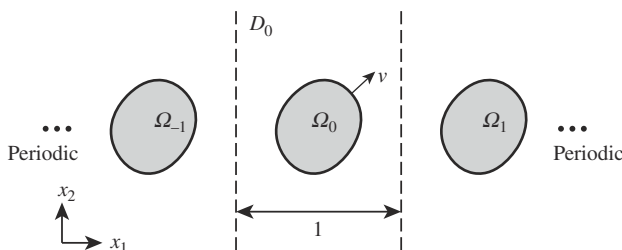
Figure 1. An infinite array of identical, equally spaced scatterers in two dimensions, i.e. a diffraction grating. Without loss of generality, the grating is aligned along the x_1-axis and the centre-to-centre spacing of adjacent scatterers is normalized to unity.

trapped mode frequency (where $\beta = \pi$). Just above the Neumann trapped mode frequency (assuming real frequencies, $k \in \mathbb{R}$), the Rayleigh–Bloch wavenumbers (i.e. point eigenvalues) move off the real axis into the complex β-plane [17], closely followed by an additional pair of complex Rayleigh–Bloch wavenumbers emerging from the continuous spectrum into the point spectrum, i.e. they 'cut on'. As frequency is increased, the additional pair of Rayleigh–Bloch wavenumbers interact with the existing pair in a manner that depends on the cylinder radius. For small cylinder radius values, after the interaction the two pairs of Rayleigh–Bloch wavenumbers become a symmetric quadruplet and have small imaginary parts, so that the corresponding Rayleigh–Bloch waves attenuate in one direction (and blow up in the other direction) as they propagate along the grating. Just below $k = 2\pi$, the Rayleigh–Bloch wavenumbers become real again at $\beta = 2\pi$ (up to a multiple of 2π), when the four complex Rayleigh–Bloch wavenumbers coalesce on the real axis, at which point the Rayleigh–Bloch waves become the Dirichlet trapped mode. This new understanding of the point spectrum connects the Neumann and Dirichlet trapped modes in frequency through generalizations of the classical Rayleigh–Bloch waves to $\beta \in \mathbb{C}$. The Rayleigh–Bloch wavenumbers vanish just above the Dirichlet trapped mode frequency, i.e. the generalized Rayleigh–Bloch waves cut off, although the exact nature of the cut-off is obscured by the continuous spectrum in the method used in [17]. We will show that the cut-off corresponds to the Rayleigh–Bloch wavenumbers swapping onto a different Riemann sheet in β-space. For large cylinder radius values, the two pairs of Rayleigh–Bloch wavenumbers appear to vanish into the continuous spectrum after interacting, which corresponds to no Dirichlet trapped mode existing for those radius values [2,8]. We will show that the Rayleigh–Bloch waves, in fact, do not cut off at this point. For frequencies $k \geq 2\pi$ (noting Bennetts & Peter [17] were only able to investigate up to $k = 3\pi$), generalized Rayleigh–Bloch waves can cut on for certain frequency intervals, depending on the radius value. In general, the structure of the problem is much more complicated beyond the Neumann trapped mode frequency and a robust method to identify Rayleigh–Bloch waves in this regime has been lacking thus far.

In this article, we recast the Rayleigh–Bloch problem in terms of the quasi-periodic Green's function. We show how Rayleigh–Bloch waves can be characterized above the Neumann trapped mode frequency and how they can be tracked for increasing frequency. In particular, we track the Rayleigh–Bloch wavenumber along different Riemann sheets and across the appropriate branch cuts (corresponding to the continuous spectrum) as frequency is varied, such that we are able to calculate and analyse more accurately the Rayleigh–Bloch waves on the main Riemann sheet (the unique Riemann sheet corresponding to standard radiation conditions), which can produce near-resonances on finite arrays in response to incident waves [18]. The key to this analysis is to allow the freedom for unbounded growth in the far-field of arbitrarily prescribed plane waves in the Green's function (and hence the solution), and to index the Riemann sheets in β-space according to the unbounded components. As in [17], results are presented for arrays of sound-hard circular scatterers with radius values $a = 0.15$,

0.25 and 0.35, which were chosen as they produce near-resonances up to order three, two and one, respectively, and, hence, their generalized Rayleigh–Bloch waves have different qualitative structures.

2. Preliminaries

(a) Problem description

We consider an infinite line of identical, equally spaced, sound-hard scatterers (i.e. a diffraction grating), embedded in a two-dimensional background medium, in which locations are defined by the Cartesian coordinate $\mathbf{x} = (x_1, x_2)$. Let the grating be aligned in the x_1-direction, the spacing of adjacent scatterers be normalized to unity, and let $\Omega_0 \subset \mathbb{R}^2$ denote the region occupied by one of the scatterers (figure 1). Therefore, the domain occupied by all scatterers along the grating is

$$\Omega^{\mathrm{P}} = \bigcup_{m \in \mathbb{Z}} \Omega_m, \quad \text{where} \quad \Omega_m = \{\mathbf{x} + m\mathbf{e_1} : \mathbf{x} \in \Omega_0\}, \tag{2.1}$$

and $\{\mathbf{e_1}, \mathbf{e_2}\}$ is the canonical basis of $\mathbb{R}^2$. The periodicity of the geometry allows the problem to be reduced to a single unit cell of unit width in the x_1-direction, infinite height in the x_2-direction and containing a single scatterer only. Without loss of generality, the problem is reduced to cell D_0, which contains scatterer Ω_0 (figure 1). For brevity, from here on the zero subscripts are dropped and the unit cell is defined as $D = \{\mathbf{x} : x_- < x_1 < x_+\}$, where $x_+ - x_- = 1$.

Time-harmonic motions are assumed at a prescribed angular frequency, $\omega \in \mathbb{R}_+$, such that the wave field at location $\mathbf{x}$ and time t is the real part of

$$u(\mathbf{x})e^{-i\omega t}, \tag{2.2}$$

where the spatial dependence, u, is to be found. It is the solution of the boundary value problem

$$\Delta u + k^2 u = 0 \quad \text{in } D \setminus \overline{\Omega}, \tag{2.3}$$

$$\nu \cdot \nabla u = 0 \quad \text{on } \partial\Omega, \tag{2.4}$$

where $k \in \mathbb{R}_+$ is the background wavenumber (which acts as a proxy for frequency, ω) and ν is the unit normal vector outward to $\Omega \equiv \Omega_0$. The spectral parameter (the Rayleigh–Bloch wavenumber) β appears in the (quasi-periodic) Bloch conditions

$$u\Big|_{x_1 = x_+} = e^{i\beta} u\Big|_{x_1 = x_-} \quad \text{and} \quad \frac{\partial u}{\partial x_1}\Big|_{x_1 = x_-} = e^{i\beta} \frac{\partial u}{\partial x_1}\Big|_{x_1 = x_-}. \tag{2.5}$$

Thus, for any pair (k, β), let the partial differential equation and boundary conditions (2.3)–(2.5) be represented by the operator equation $F(k, \beta)u = 0$. The solution space is restricted, such that

$$u \text{ is bounded as } x_2 \to \pm\infty, \tag{2.6}$$

where the limit denotes the far-field of the grating.

When seeking classical Rayleigh–Bloch waves, the far-field condition (2.6) is constrained to

$$u \to 0 \text{ as } x_2 \to \pm\infty, \tag{2.7}$$

and, hence, the solution space is restricted. By contrast, in the scattering problem, the far-field condition is modified to the radiation condition

$$u - u^{\mathrm{in}} \text{ is outgoing as } x_2 \to \pm\infty, \tag{2.8}$$

where u^{in} is a prescribed incident wave field that determines β, so that it is no longer a spectral parameter. For a plane incident wave field

$$u^{\text{in}}(\mathbf{x}) = \exp\{ik(\cos(\psi)x_1 + \sin(\psi)x_2)\}, \tag{2.9}$$

where $\psi \in [-\pi, \pi)$ is its angle to the positive x_1-axis, and, thus, $\beta = k\cos(\psi)$ is enforced.

Note from (2.5) that addition of integer multiples of 2π to β leaves the problem unchanged. Moreover, there is $\pm\beta$-symmetry for the circular scatterers considered in the numerical results (or, more generally, any scatterer symmetric with respect to the x_2-axis). For such cases, it is standard to restrict analysis to the *first irreducible Brillouin zone*, $\beta \in [0, \pi]$, although the Brillouin zone restriction will be removed when the problem is generalized from §4 onwards.

(b) Plane-wave expansion

Consider the regions

$$D_\pm = \{x \in \mathbb{R} : \pm x_2 > H\} \subset D, \tag{2.10}$$

with $H > 0$ chosen such that $\Omega \cap D_\pm = \varnothing$, i.e. the regions are above (+) and below (−) the scatterer. A solution of the Helmholtz equation (2.3) in $\Omega_\pm$, which satisfies the Bloch conditions (2.5), is sought in the plane-wave form $e^{i\mathbf{K}\cdot\mathbf{x}}$. The *Bloch wavevector* $\mathbf{K} \equiv (K_1, K_2) \in \mathbb{C}^2$ has magnitude, $|\mathbf{K}| \equiv K_1^2 + K_2^2$, such that

$$K_1^2 + K_2^2 = k^2, \tag{2.11}$$

to satisfy the Helmholtz equation, and a first component of the form

$$K_1 = \beta + 2m\pi =: k_m \quad \text{for} \quad m \in \mathbb{Z}, \tag{2.12}$$

to satisfy the Bloch conditions. Therefore, let

$$K_2 = \sqrt{k^2 - k_m^2}, \tag{2.13}$$

where the square root $z \in \mathbb{C} \mapsto \sqrt{z} \in \mathbb{C}$ is defined as

$$\sqrt{z} = \sqrt{|z|}\exp\left(\frac{i}{2}\text{Arg}\,z\right) \quad \text{where} \quad \text{Arg} : \mathbb{C} \to [-\pi, \pi). \tag{2.14}$$

This places the branch cut on the negative real axis, ensures the square root maps to complex numbers with non-negative real parts, and that the square root of a negative real number maps to the imaginary axis in the lower half complex plane.

In the Rayleigh–Bloch problem (or the scattered problem in which u is replaced by $u - u^{\text{in}}$), the wave field has the plane-wave expansion

$$u(\mathbf{x}) = \sum_{m \in \mathbb{Z}} c_m^\pm e^{ik_m x_1 \mp \sqrt{k_m^2 - k^2}\,x_2}, \tag{2.15}$$

$$= \sum_{m \in \mathcal{M}} c_m^\pm e^{ik_m x_1 \pm i\sqrt{k^2 - k_m^2}\,x_2} + \sum_{m \in \mathbb{Z} \setminus \mathcal{M}} c_m^\pm e^{ik_m x_1 \mp \sqrt{k_m^2 - k^2}\,x_2} \quad \text{in } D_\pm, \tag{2.16}$$

where the set $\mathcal{M} \subset \mathbb{Z}$ contains the indices for which $K_2 \in \mathbb{R} \geq 0$, and the coefficients $c_m^\pm \in \mathbb{C}$ ($m \in \mathbb{Z}$) are to be found. Equation (2.16) expresses the scattered field as outgoing propagating waves ($m \in \mathcal{M}$; $K_1, K_2 \in \mathbb{R}$) and decaying waves ($m \in \mathbb{Z} \setminus \mathcal{M}$; $K_1 \in \mathbb{R}$, $K_2 \notin \mathbb{R}$). Classical Rayleigh–Bloch waves exist in a regime for which there are no outgoing propagating waves, $\mathcal{M} = \varnothing$. By contrast, in the scattering problem there is at least one outgoing propagating wave, $\mathcal{M} \neq \varnothing$, and the directions of the plane waves for $m \in \mathcal{M}$ are known as the *scattering angles* [19,20]. The scattering angles contain only the incident wave angle, ψ, for $k < \pi$ ($\mathcal{M} = \{0\}$). For $\pi < k < 2\pi$, an additional scattering angle is possible for certain incident directions, and so on.
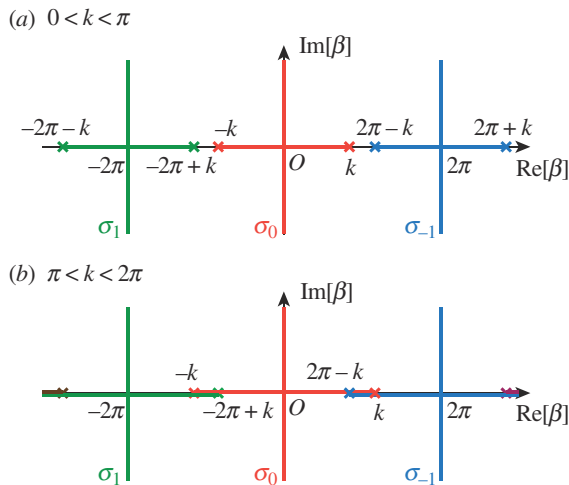
(*a*) $0 < k < \pi$

(*b*) $\pi < k < 2\pi$

Figure 2. Continuous spectrum in complex β-space, σ_{cts} (3.1), which corresponds to branch cuts of the Green's function with associated branch points (crosses). (*a*) For $0 < k < \pi$, the subsets are disjoint, but for (*b*) $\pi < k < 2\pi$ they overlap on the real β-axis.

(c) Quasi-periodic Green's function and boundary integral equation

Let G_β be the quasi-periodic Green's function, i.e. $G_\beta(\,\cdot\,, \mathbf{y})$ solves the Helmholtz equation

$$\Delta_x G_\beta(\mathbf{x}, \mathbf{y}) + k^2 G_\beta(\mathbf{x}, \mathbf{y}) = 0, \quad x \in \mathbb{R}^2 \setminus \{\mathbf{y} + m\mathbf{e}_1 : m \in \mathbb{Z}\}, \mathbf{y} \in \mathbb{R}^2 \tag{2.17a}$$

with the logarithmic singularity $G_\beta(\mathbf{x}, \mathbf{y}) = O(\log |\mathbf{x} - \mathbf{y}|)$ as $|\mathbf{x} - \mathbf{y}| \to 0$. Further, it satisfies the Bloch conditions

$$G_\beta\Big|_{x_1 = x_+} = \mathrm{e}^{\mathrm{i}\beta} G_\beta\Big|_{x_1 = x_-} \quad \text{and} \quad \frac{\partial G_\beta}{\partial x_1}\Big|_{x_1 = x_+} = \mathrm{e}^{\mathrm{i}\beta} \frac{\partial G_\beta}{\partial x_1}\Big|_{x_1 = x_-} \tag{2.17b}$$

and the far-field radiation condition

$$G_\beta \text{ is bounded and outgoing as } x_2 \to \pm\infty. \tag{2.17c}$$

The quasi-periodic Green's function is used to formulate the Brakhage–Werner boundary integral equation

$$2\frac{\partial}{\partial\nu(\mathbf{x})} \int_{\partial\Omega} \frac{\partial G_\beta}{\partial\nu(\mathbf{y})}(\mathbf{x}, \mathbf{y})\varphi(\mathbf{y})\mathrm{d}s(\mathbf{y}) - 2\mathrm{i}\eta \int_{\partial\Omega} \frac{\partial G_\beta}{\partial\nu(\mathbf{x})}(\mathbf{x}, \mathbf{y})\varphi(\mathbf{y})\mathrm{d}s(\mathbf{y}) + \mathrm{i}\eta\varphi(\mathbf{x}) = 0 \tag{2.18}$$

for $\mathbf{x} \in \partial\Omega$, and with arbitrary constant $\eta > 0$. Equation (2.18) is solved for the density φ for $\mathbf{x} \in \partial\Omega$ (see appendix B). The solution, u, of the quasi-periodic problem (2.3)–(2.6) is then obtained from

$$u(\mathbf{x}) = \int_{\partial\Omega} \left(\frac{\partial G_\beta}{\partial\nu(\mathbf{y})}(\mathbf{x}, \mathbf{y}) - \mathrm{i}\eta G_\beta(\mathbf{x}, \mathbf{y}) \right)\varphi(\mathbf{y})\mathrm{d}s(\mathbf{y}), \quad \mathbf{x} \in \mathbb{R}^2 \setminus \overline{\Omega^{\mathrm{P}}}. \tag{2.19}$$

Solutions are calculated numerically by discretizing the boundary integral equation (2.18). The approximate (discrete) form of (2.18) is expressed as (see appendix B)

$$\mathcal{A}\boldsymbol{\varphi} = \mathbf{0}, \tag{2.20}$$

where $\mathcal{A}(k, \beta)$ is a $2N \times 2N$ square matrix with known entries, and $\boldsymbol{\varphi}(k, \beta)$ is a column vector containing the unknown density at discrete points along the boundary.
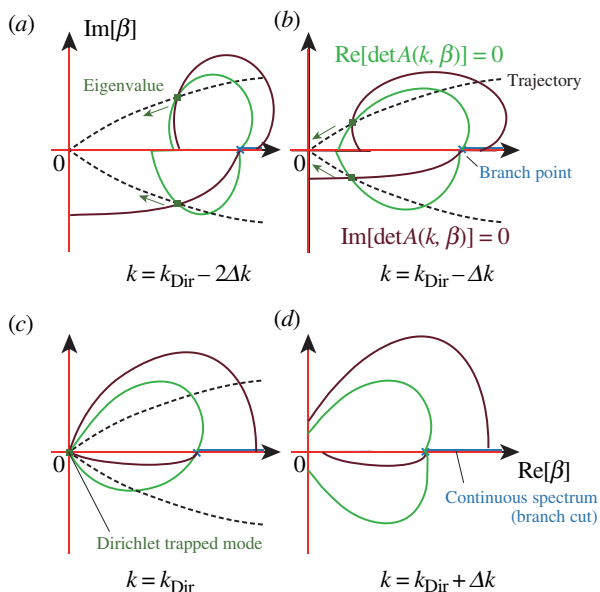
Figure 3. Schematic illustration of the trajectory of an eigenvalue (crossing of the two contours $\mathrm{Re}[\det \mathcal{A}(k, \beta)] = 0$ and $\mathrm{Im}[\det \mathcal{A}(k, \beta)] = 0$) as frequency increases. (c) The eigenvalue is embedded in the continuous spectrum at $k = k_{\mathrm{Dir}}$. (d) The eigenvalues disappear from the complex β-plane for $k > k_{\mathrm{Dir}}$.

3. Spectral properties of gratings

(a) Continuous spectrum

The *continuous spectrum*, $\sigma_{\mathrm{cts}}(k)$, contains β-values supporting non-trivial solutions to $Fu = 0$ that are bounded in the far-field (2.6) but do not tend to zero. Thus, seeking $\mathcal{M} \neq \varnothing$ in (2.16), the continuous spectrum is given by (figure 2)

$$\sigma_{\mathrm{cts}}(k) := \{\beta \in \mathbb{C} : \exists \, m \in \mathbb{Z} : k^2 - k_m^2 \in \mathbb{R} \text{ and } k^2 - k_m^2 > 0\}$$
$$=: \bigcup_{m \in \mathbb{Z}} \sigma_m(k), \tag{3.1}$$

where the subsets are

$$\sigma_m(k) = \{-2m\pi + \xi : -k < \xi < k\} \cup \{-2m\pi \pm i\xi : \xi > 0\}. \tag{3.2}$$

The first set on the right-hand side of (3.2) are the well-known components of the continuous spectrum that correspond to β-values for the problem of scattering by a plane incident wave (2.8) for incident angles $\psi \in (-\pi, 0)$ [2]. Grazing incidence ($\psi = -\pi, 0$) occurs when $\xi = \pm k$, for which the solution is trivial [9] and, hence, not included in the spectrum. The second set contains the less well-known components of the continuous spectrum that represent solutions to a generalized scattering problem in which the modulus of the incident field grows/decays in the x_1-direction (noting that x_1 is bounded in the unit cell), i.e. $K_1 \in i\mathbb{R}$ and $K_2 \in \mathbb{R}_+$ [11,17]. Note that the subsets of the continuous spectrum are disjoint for $k < \pi$ (figure 2a), but that they overlap on the real β-axis for $k > \pi$ (figure 2b), where the number of overlaps corresponds to the number of scattering angles in the corresponding scattering problem.

(b) Point spectrum and embedded eigenvalues

The focus of this study is on the point spectrum, $\sigma_{\mathrm{pt}}(k)$ for $k \in \mathbb{R}_+$. As standard, the point spectrum contains $\beta \in \mathbb{C}$ for which solutions of $Fu = 0$ exist that tend to zero in the far-field (2.7), i.e. the Rayleigh–Bloch wave problem. Except for embedded eigenvalues (see below), the point spectrum contains β-values for which $\mathcal{M} = \varnothing$ in (2.16). Thus, the point spectrum is

$$\sigma_{\mathrm{pt}}(k) \subset \{\beta \in \mathbb{C} : \nexists\, m \in \mathbb{Z} : k^2 - k_m^2 \in \mathbb{R} \text{ and } k^2 - k_m^2 \geq 0\} \cup \sigma_{\mathrm{em}}(k), \tag{3.3}$$

where $\sigma_{\mathrm{em}}(k)$ denotes the set of embedded eigenvalues, which typically is $\sigma_{\mathrm{em}}(k) = \varnothing$.

The members of the point spectrum coincide with the eigenvalues, $\beta(k)$, of $\mathcal{A}(k, \beta)$. Thus, the formulation (2.20) explicitly separates the point spectrum from the continuous spectrum, which is essential for the tracking of the Rayleigh–Bloch waves (§5). Admissible values of $\beta \in \sigma_{\mathrm{pt}}(k)$ are found as the intersections of

$$\mathrm{Re}[\det \mathcal{A}(k, \beta)] = 0 \quad \text{and} \quad \mathrm{Im}[\det \mathcal{A}(k, \beta)] = 0, \tag{3.4}$$

i.e. as the eigenvalues of the boundary integral equation (2.18). For circular scatterers with radius $a = 0.25$ and $k \in (\pi, 2\pi)$, there are typically two point spectrum eigenvalues (Rayleigh–Bloch wavenumbers) in the first irreducible Brillouin zone, $\mathrm{Re}[\beta] \in [0, \pi]$ (figure 3; [17]). As frequency increases, the eigenvalues move towards the origin (figure 3a,b) until they coalesce at $\beta = 0$ for the frequency $k = k_{\mathrm{Dir}} \approx 1.955$ (figure 3c). At this frequency, they become the Dirichlet trapped modes [8], which are members of the point spectrum embedded in the continuous spectrum, as $k^2 - k_0^2 \in \mathbb{R} \geq 0$, so that $\beta = 0 \in \sigma_{\mathrm{em}}(k_{\mathrm{Dir}})$. For frequencies just above k_{Dir}, the point spectrum appears to be empty (figure 3d).

4. Indexing Riemann sheets

(a) Family of quasi-periodic Green's functions

Let requirement (2.17c) on the quasi-periodic Green's function in the far-field be dropped. The solutions of the remaining field equation (2.17a) and quasi-periodicity conditions (2.17b) form an infinite family of quasi-periodic Green's functions, $\{G_\beta(\mathbf{x}, \mathbf{y}; I)\}$. The family is parametrized by the index set I (a bounded subset of $\mathbb{Z}$), such that

$$\begin{aligned}
G_\beta(\mathbf{x}, \mathbf{y}; I) = {} & \sum_{m \in I} \frac{-1}{2\sqrt{k_m^2 - k^2}} \exp\left(ik_m(x_1 - y_1)\right) \exp\left(\sqrt{k_m^2 - k^2}|x_2 - y_2|\right) \\
& + \sum_{m \notin I} \frac{1}{2\sqrt{k_m^2 - k^2}} \exp\left(ik_m(x_1 - y_1)\right) \exp\left(-\sqrt{k_m^2 - k^2}|x_2 - y_2|\right).
\end{aligned} \tag{4.1}$$

Equation (4.1) is similar to the standard plane-wave expansion for the quasi-periodic Green's function [21] but where a finite number of the plane waves are permitted to be unbounded in the far-field ($m \in I$). The choice $I = \varnothing$ returns the bounded quasi-periodic Green's function, which is used to solve for classical Rayleigh–Bloch waves and the scattering problem (§2c). All other quasi-periodic Green's functions in the family ($I \neq \varnothing$) are unbounded in the far-field for $\beta \notin \sigma_{\mathrm{cts}}$.

(b) Bounded and unbounded solutions

Let the non-trivial solutions of the unforced problem be $u(\mathbf{x}; I)$, where the index set I connects the solutions with the corresponding quasi-periodic Green's functions (4.1). Substituting (4.1) into (2.19) gives the plane-wave expansions

$$u(\mathbf{x}; I) = \sum_{m \in I} c_m^{\pm}(I) \mathrm{e}^{\mathrm{i}k_m x_1 \pm \sqrt{k_m^2 - k^2} x_2} + \sum_{m \notin I} c_m^{\pm}(I) \mathrm{e}^{\mathrm{i}k_m x_1 \mp \sqrt{k_m^2 - k^2} x_2} \quad \text{for} \quad \mathbf{x} \in D_{\pm}, \tag{4.2}$$

where

$$c_m^{\pm}(I) = \frac{-1}{2\sqrt{k_m^2 - k^2}} \int_{\partial\Omega} \varphi(\mathbf{y}) \left(\frac{\partial}{\partial\nu(y)} - \mathrm{i}\eta \right) \mathrm{e}^{-\mathrm{i}k_m y_1 \mp \sqrt{k_m^2 - k^2} y_2} \mathrm{d}s(\mathbf{y}) \quad \text{for} \quad m \in I, \tag{4.3a}$$

$$\text{and} \quad c_m^{\pm}(I) = \frac{1}{2\sqrt{k_m^2 - k^2}} \int_{\partial\Omega} \varphi(\mathbf{y}) \left(\frac{\partial}{\partial\nu(y)} - \mathrm{i}\eta \right) \mathrm{e}^{-\mathrm{i}k_m y_1 \pm \sqrt{k_m^2 - k^2} y_2} \mathrm{d}s(\mathbf{y}) \quad \text{for} \quad m \notin I. \tag{4.3b}$$

Equation (4.2) partitions the solution into plane waves that are potentially unbounded in the far-field ($m \in I$) and bounded ($m \notin I$), i.e. their boundedness in the far-field is equivalent to that of the corresponding quasi-periodic Green's functions. Therefore, $u(\mathbf{x}; I = \varnothing)$ is bounded in the far-field and referred to as a bounded solution, whereas $u(\mathbf{x}; I \neq \varnothing)$ is (typically) unbounded in the far-field and referred to as an unbounded solution.

(c) Riemann surfaces in complex β-space

The quasi-periodic Green's functions (4.1) possess branch cuts, which are induced by the square-root functions. The branch cuts coincide with the continuous spectrum, where the mth subset of the continuous spectrum, σ_m, corresponds to the branch cut for the mth plane wave in the Green's function. Thus, σ_m will be referred to as the mth branch cut (as well as a subset of the continuous spectrum). The real parts of the branches are bounded by branch points, $\beta = k + 2m\pi$ ($m \in \mathbb{Z}$), which correspond to grazing incidence in the scattering problem.

The branch cuts connect the different members of the quasi-periodic Green's function family. First consider $k < \pi$, for which the branch cuts σ_m ($m \in \mathbb{Z}$) are disjoint (figure 2a). In this case, the mth branch cut connects the bounded Green's function, $G_\beta(\mathbf{x}, \mathbf{y}; I = \varnothing)$, with the unbounded Green's function $G_\beta(\mathbf{x}, \mathbf{y}; I = \{m\})$. More generally, the mth branch cut connects $G_\beta(\mathbf{x}, \mathbf{y}; I)$ for an index set not containing m ($I \cap \{m\} = \varnothing$) with $G_\beta(\mathbf{x}, \mathbf{y}; I \cup \{m\})$. These are referred to as *first-order connections*. For $k > \pi$, the branch cuts overlap on the real β-axis (figure 2b), which can create higher order connections. For instance, if branch cuts $\sigma_m, \sigma_{m+1}, \ldots, \sigma_{m+n}$ overlap, then their overlapping interval creates an nth-order connection between $G_\beta(\mathbf{x}, \mathbf{y}; I)$ and $G_\beta(\mathbf{x}, \mathbf{y}; J)$, where

$$J = (I \cup \{m, m+1, \ldots, m+n\}) \setminus (I \cap \{m, m+1, \ldots, m+n\}). \tag{4.4}$$

Therefore, the family of quasi-periodic Green's functions are interpreted as Riemann sheets (figure 4), connected by branch cuts.

The quasi-periodic Green's functions contain propagating wave components on the branch cuts. For example, consider the sheet $I = \varnothing$ and disjoint branch cuts ($k < \pi$), then as β approaches the branch cut σ_0 from either the first or third quadrants of the complex β-plane, the wavenumber of the zeroth plane wave in the x_2-direction is such that

$$-\sqrt{k_0^2 - k^2} \to -\mathrm{i}q_0 \quad \text{where} \quad q_0 \in \mathbb{R}_+, \tag{4.5}$$

i.e. the $m = 0$ plane wave in the Green's function tends to an incoming, propagating wave. In contrast, as β approaches the branch cut from the second or fourth quadrants, the $m = 0$ plane wave tends to an outgoing, propagating wave. Similar patterns occur for the other branch cuts. For $k > \pi$, as β approaches an overlapping interval of the branch cuts from any direction, the corresponding plane waves in the Green's function must be a combination of incoming and outgoing plane waves.
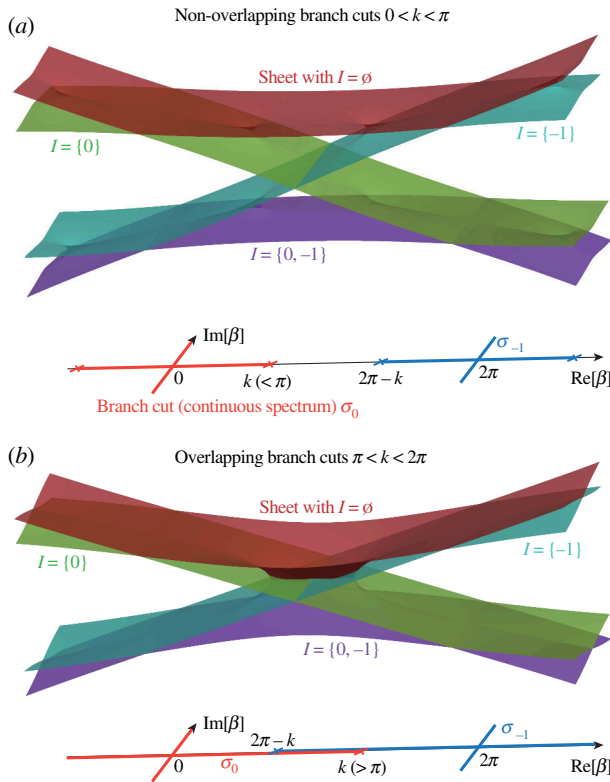
Figure 4. Schematic interpretation of quasi-periodic Green's functions as Riemann sheets, connected by branch cuts (σ_m).

5. Tracking Rayleigh–Bloch waves

(a) Block Sakurai–Sugiura method

The block Sakurai–Sugiura method (SSM) [22] is used to find pairs (β, φ), where $\beta \in \mathbb{C}$ and $\varphi \in \mathbb{C}^{2N} \setminus \{0\}$, such that φ solves the homogeneous version of system (2.20) ($f \equiv 0$) for a given frequency $k > 0$ and index set I. Let $\mathcal{C}$ be a Jordan curve in $\mathbb{C}$, then the block SSM finds eigenvalues β inside $\mathcal{C}$ and corresponding φ, using contour integrals of the form

$$\mu_l := \int_{\mathcal{C}} z^l U^H \mathcal{A}^{-1}(k, \beta) W \, dz \quad \text{for} \quad l = 0, 1, \ldots, 2Q - 1, \tag{5.1}$$

where $U \in \mathbb{C}^{2N \times P}$ and $W \in \mathbb{C}^{2N \times P}$ are full column-rank matrices for a chosen integer $P \leq 2N$, and Q is a sufficiently large integer. The moments $\mu_l \in \mathbb{C}^{P \times P}$ are used to construct the block Hankel matrices

$$H := \begin{bmatrix} \mu_0 & \mu_1 & \cdots & \mu_{Q-1} \\ \mu_1 & \mu_2 & \cdots & \mu_Q \\ \vdots & \vdots & \ddots & \vdots \\ \mu_{Q-1} & \mu_Q & \cdots & \mu_{2Q-2} \end{bmatrix} \quad \text{and} \quad H^< := \begin{bmatrix} \mu_1 & \mu_2 & \cdots & \mu_Q \\ \mu_2 & \mu_3 & \cdots & \mu_{Q+1} \\ \vdots & \vdots & \ddots & \vdots \\ \mu_Q & \mu_{Q+1} & \cdots & \mu_{2Q-1} \end{bmatrix}. \tag{5.2}$$

The block SSM asserts that all β inside $\mathcal{C}$, such that

$$\det \mathcal{A}(k, \beta) = 0, \tag{5.3}$$

are eigenvalues $\lambda = \beta$ of the pencil

$$\lambda \mapsto H - \lambda H^{<}, \tag{5.4}$$

which is computed using standard numerical linear algebra. The corresponding eigenvectors, φ, are found from the null space of $\mathcal{A}(k, \beta)$.

(b) Swapping between Riemann sheets

Eigenvalue trajectories are calculated based on the assumption that $\beta(k)$ moves continuously on the Riemann sheets as frequency varies. Suppose (β_i, Ψ^i) is a known eigenpair for given frequency $k = k_i > 0$ and index set I_i. The block SSM is used to seek the eigenpair $(\beta_{i+1}, \Psi^{i+1})$ at $k = k_{i+1} := k_i + \delta$, where $\delta \in \mathbb{R}$ is a small frequency increment, and using a contour path $\mathcal{C}$ containing β_i (figure 5a).

The above approach can be applied in a relatively straightforward manner until an eigenvalue reaches a branch cut and swaps onto a different Riemann sheet. Thus, on a given Riemann sheet (e.g. $I = \varnothing$), eigenvalues can cut on or cut off at certain critical frequencies [17]. In cases where an eigenvalue on a Riemann surface corresponding to index set I_i is close to a branch cut (or branch cuts) and may swap between Riemann sheets over a small frequency step, the contour path, $\mathcal{C}$, is set to intersect the relevant branch cut (figure 5a). (For simplicity, it is assumed $\mathcal{C}$ does not contain any branch points, although the assumption can be removed by performing the contour integration along a closed curve encircling a branch point twice instead of a Jordan curve.) The branch cut separates the closed path $\mathcal{C}$ into open curves ($\mathcal{C}^0$, $\mathcal{C}^1$ and $\mathcal{C}^2$ in figure 5a), each of which corresponds to an index set ($I^0 = I_i$, I^1 and I^2). Then, the block SSM is performed using the moments

$$\mu_l = \sum_j \int_{\mathcal{C}^j} z^l U^H \mathcal{A}^{-1}(k, \beta; I^j) W \, \mathrm{d}z. \tag{5.5}$$

This algorithm finds an eigenvalue $(\beta_{i+1}, \Psi^{i+1})$ if the path $\mathcal{C}$ is sufficiently large (or δ is small) so that it contains β_{i+1}. The index set I^{i+1} is determined by the location of β_{i+1} in the complex β-plane. The approach can be viewed as making the contour path continuous over the Riemann sheets.

For circular scatterers of radius $a = 0.25$, eigenvalues are found on the sheet $I = \varnothing$ (Rayleigh–Bloch wavenumbers) close to the origin ($\beta = 0$) just below the Dirichlet trapped mode frequency, $k = k_{\mathrm{Dir}} \approx 1.9555\pi$, and moving towards the origin as frequency increases (figure 6a,b). The eigenvalues are close to branch cuts σ_{-1} and σ_0 and an interval along which they overlap, but no eigenvalues appear close to the origin on the neighbouring sheets ($I = \{0\}$, $\{-1\}$ and $\{0, -1\}$; figure 6a,b). The eigenvalues coalesce at the origin for $k = k_{\mathrm{Dir}}$, which occurs on both the sheets with $I = \varnothing$ and $I = \{0\}$ (figure 6c). For frequencies just above $k = k_{\mathrm{Dir}}$, the eigenvalues swap to the sheet with $I = \{0\}$ (Rayleigh–Bloch wavenumbers cut off; figure 6d).

6. Results

Results are shown to explain the cutting off and on of Rayleigh–Bloch waves on the sheet with $I = \varnothing$, as frequency varies [17], and to explore the behaviours at higher frequencies than [17]. Therefore, for consistency with [17], the scatterers are restricted to being circular, such that

$$\Omega = \{(x_1, x_2) : x_1^2 + x_2^2 \le a^2\} \quad \text{and} \quad x_\pm = \pm 0.5, \tag{6.1}$$

where $a \in (0, 0.5)$ is the radius. Gratings consisting of small scatterers ($a = 0.15$), intermediate scatterers ($a = 0.25$) and large scatterers ($a = 0.35$) are considered, as in [17].
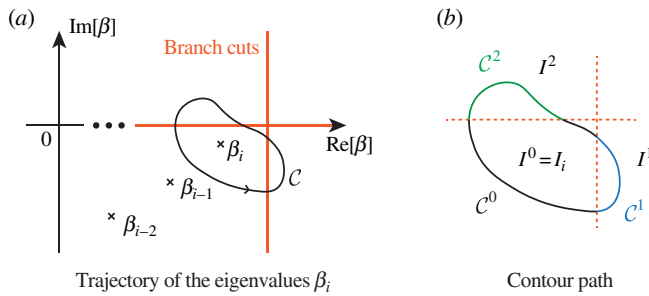
Figure 5. Trajectory of the eigenvalues β_i and the contour path $\mathcal{C}$. The path $\mathcal{C}$ is cut into several pieces along the branch cuts.

(a) Case study

The grating of intermediate scatterers is used for a detailed case study (figure 7). The trajectories are divided into four groups (denoted by blue, red, green and cyan curves) over seven Riemann sheets (figure 7a–g), with capital letters denoting points of interest along the trajectories. The first Brillouin zone is shown ($0 \leq \mathrm{Re}(\beta) < 2\pi$), rather than the first irreducible Brillouin zone ($0 \leq \mathrm{Re}(\beta) < \pi$) for a better overall picture of the trajectories. Primed letters are used, where appropriate, to denote the symmetric complements of the eigenpairs at the non-primed letters, i.e. the $2\pi - \beta$ solutions.

Starting on the sheet with $I = \varnothing$ (figure 7a), classical Rayleigh–Bloch waves ($\beta \in \mathbb{R}$) exist at low frequencies (red curves starting at points A and A′). In the first irreducible Brillouin zone ($0 \leq \mathrm{Re}(\beta) < \pi$), there is an eigenvalue corresponding to a rightwards propagating Rayleigh–Bloch wave (e.g. the eigenvalue at point A). The symmetric complement (in $\pi \leq \mathrm{Re}(\beta) < 2\pi$, e.g. point A′) corresponds to a leftwards propagating Rayleigh–Bloch wave. They sit between the branches σ_0 and σ_{-1} ($\beta > k$), and close to the branch points (the tips of the branches on the real β-axis), e.g. $\beta = 0.032\pi$ when $k = 0.030\pi$ (point A). As frequency increases, the Rayleigh–Bloch wavenumbers (point eigenvalues) move along horizontal trajectories on the real β-axis towards $\beta = \pi$, remaining ahead of the branch points. The eigenvalues for the rightwards and leftwards propagating Rayleigh–Bloch waves coalesce at $\beta = \pi$ when $k = 0.886\pi$ (point B), at which point they correspond to a standing wave (the Neumann trapped mode; figure 7h). They then become a complex conjugate pair that veer away from one another on vertical trajectories. This behaviour is analogous to the transition from a passband to a bandgap in periodic media where only point spectra exist. They reach maximum distances from the real axis when $k = 1.011\pi$ (points C and $\overline{\mathrm{C}}$, where overbars replace primes to emphasize the complex conjugate relationship) before retracing their paths back towards the real axis. The eigenvalues in the upper and lower halves of the complex plane support modes that decay rightwards and leftwards along the array, respectively.

Just above the frequency at which the eigenvalues that continuously extend the classical Rayleigh–Bloch wavenumbers (red curves) start moving back towards the real β-axis ($k = 1.011\pi$), a second pair of Rayleigh–Bloch wavenumbers (point eigenvalues) cut onto the sheet with $I = \varnothing$ from $\beta = \pi$. The new wavenumber pair have swapped onto the sheet with $I = \varnothing$ from the neighbouring sheet with index set $I = \{-1,0\}$ (figure 7d), i.e. they come from a second-order connection through a point where the branch cuts σ_{-1} and σ_0 overlap. Before they swap onto the sheet with $I = \varnothing$, the behaviour of the eigenvalue pair on the sheet with $I = \{-1,0\}$ is similar to that of the classical Rayleigh–Bloch wavenumbers on the sheet with $I = \varnothing$ (passband to bandgap type behaviour; green curves and arrows in figure 7d). At low frequencies, the eigenvalues are real-valued (e.g. F and F′) and move along horizontal trajectories towards $\beta = \pi$ as frequency increases, where they coalesce just below $k = \pi$ (G), i.e. before the branch cuts reach this point. They then form a complex conjugate pair and veer away from
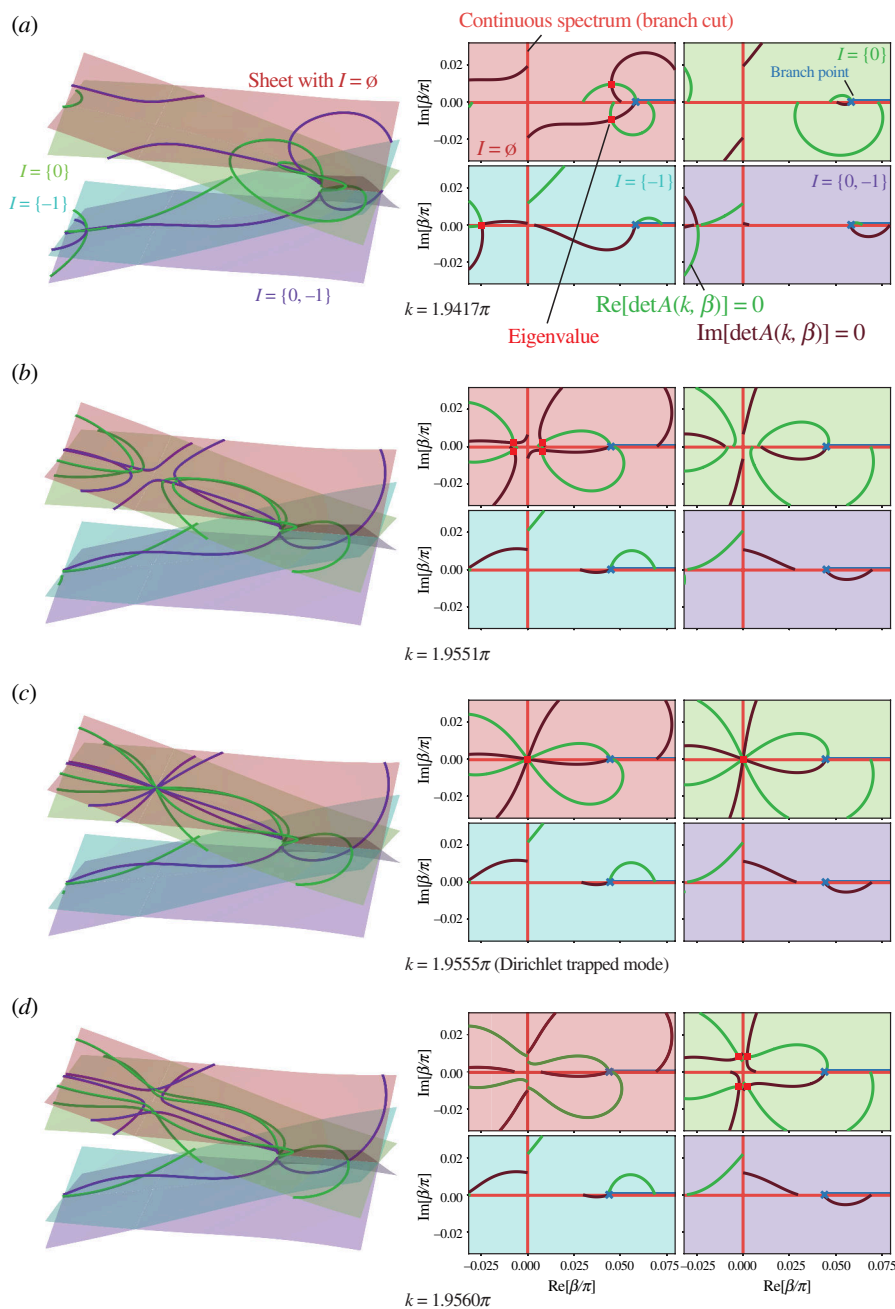
Figure 6. Contour lines of $\mathrm{Re}[\det\mathcal{A}(k,\beta)] = 0$ (green) and $\mathrm{Im}[\det\mathcal{A}(k,\beta)] = 0$ (brown) for circular scatterers of radius $a = 0.25$ and a series of frequencies on the sheets $I = \varnothing, \{0\}, \{-1\}$ and $\{0,-1\}$. The left-hand side panels illustrate the Riemann sheets, and the right-hand side panels show projections onto complex β-planes indexed by I. The crossing of the contours indicates the existence of eigenvalues β (red bullets).

one another along vertical trajectories to some maximum points (H and $\overline{\mathrm{H}}$) before moving back along the vertical trajectories towards one another (and the real axis). Their trajectories meet again in complex β-space at $\beta = \pi$ when $k = 1.116\pi$ (point I), i.e. after σ_{-1} and σ_0 have reached this point, so that the eigenvalues do not meet on the Riemann sheets and, instead, swap onto the sheet with $I = \varnothing$. While the eigenvalues are on the sheet with $I \neq \varnothing$, their corresponding
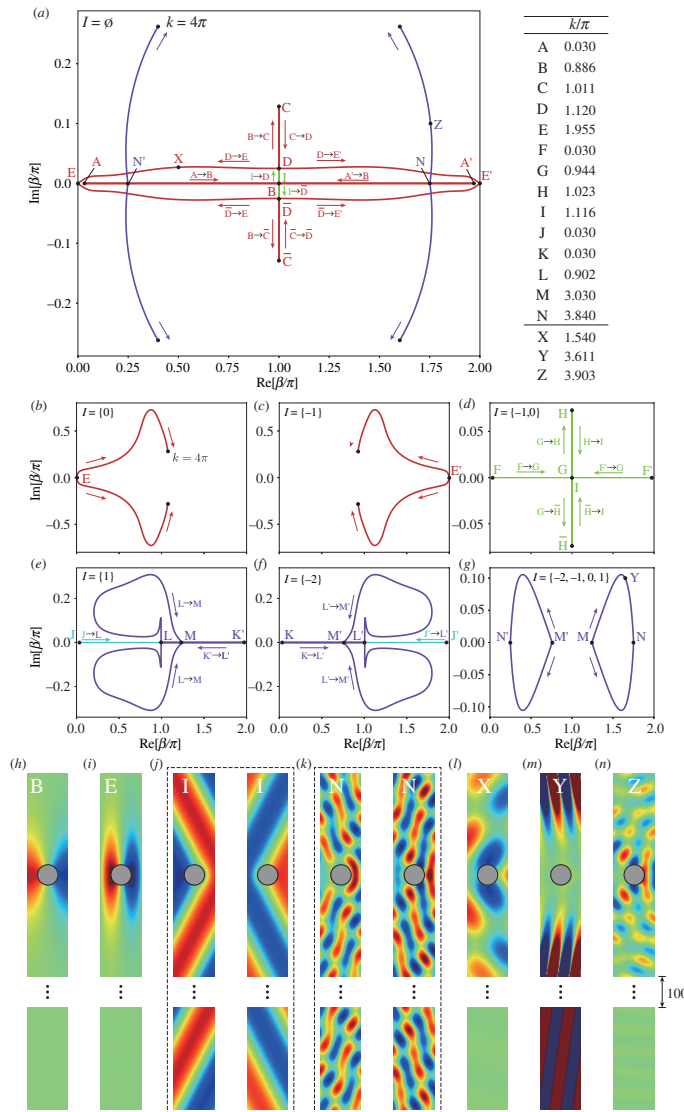
Figure 7. Trajectories of some eigenvalues on some sheets indexed by I in the case of $a = 0.25$. Some representative points on the trajectories are marked by the letters. The corresponding frequencies are listed on the right-top table. The bottom figures show the real part of the eigenmodes associated with the eigenvalue indicated by the letters.

modes are unbounded in the far-field. At the point the eigenvalues swap to the sheet with $I = \varnothing$ ($k = 1.116\pi$; point I), they lie on branch cuts (σ_{-1} and σ_0). Their corresponding modes are of the form

$$u(\mathbf{x}) \sim c_{-1}\, e^{i\pi(-x_1 + 0.4937x_2)} + c_0\, e^{i\pi(x_1 - 0.4937x_2)} \quad \text{as} \quad x_2 \to \pm\infty \tag{6.2}$$

so that they are bounded in the far-field but not decaying (figure 7j), i.e. they are not point eigenvalues. The eigenvalues become Rayleigh–Bloch wavenumbers on the sheet with $I = \varnothing$ that move on vertical trajectories for frequencies just above $k = 1.116\pi$ (green curves in figure 7a), so that they are complex-valued point eigenvalues as their corresponding modes decay in the far-field.

The second pair of Rayleigh–Bloch wavenumbers move on vertical trajectories for only a short frequency interval (up to $k = 1.120\pi$) before they collide with the existing pair of

Rayleigh–Bloch wavenumbers (at points D and $\overline{\mathrm{D}}$ in figure 7a). The trajectories of the four Rayleigh–Bloch wavenumbers then become locked, such that they form a set $\beta = \pi \pm \beta_r \pm i\epsilon$ for $\beta_r \in [0, \pi]$ and $\epsilon \approx 0.03\pi$. The locked trajectories cannot be unambiguously connected with those below the collisions and, thus, they are considered to belong to the same group (all red curves). They move along trajectories almost parallel to the real β-axis (β_r increasing and ϵ approximately constant), just behind the branch points (for σ_{-1} and σ_0, not shown) until $k \approx 1.540\pi$. For this frequency interval, the corresponding modes extend farther from the array than classical Rayleigh–Bloch wave but, nevertheless, decay in the far-field (e.g. figure 7l). They then move towards the real β-axis (β_r increasing and ϵ decreasing), overtaking the branch points ($\beta_r > k - \pi$), and coalesce at $\beta = 0$ and 2π when $k = 1.955\pi$ (points E and E′). The eigenvalues lie on branch cuts (σ_0 at E and σ_{-1} at E′), but are at points that allow the eigenvalues to coalesce on the sheet with $I = \varnothing$. The corresponding (degenerate) mode has a propagating plane-wave component ($\mathcal{M} \neq \varnothing$) but its amplitude is (numerically) zero, so that the mode (the Dirichlet trapped mode) decays in the far-field (figure 7i). Thus, these are embedded point eigenvalues. They then swap onto sheets with $I = \{0\}$ and $\{-1\}$ (figure 7b,c), where they remain locked as complex conjugate pairs up to the highest frequency considered ($k = 4\pi$).

There are no Rayleigh–Bloch wavenumbers (eigenvalues on the sheet with $I = \varnothing$) above the Dirichlet trapped mode frequency ($k = 1.955\pi$) until just below $k = 4\pi$. At $k = 3.840\pi$, a pair of eigenvalues cut onto the sheet with $I = \varnothing$ on the real β-axis (point N in figure 7a), along with a complementary pair of eigenvalues (point N′). The corresponding modes are of the form

$$u(\mathbf{x}) \sim c_{-2}\,e^{i\pi(-2.248x_1 \pm 3.113x_2)} + c_{-1}\,e^{i\pi(-0.2485x_1 \pm 3.832x_2)}$$

$$+ c_0\,e^{i\pi(1.752x_1 \mp 3.417x_2)} + c_1\,e^{i\pi(3.752x_1 \mp 0.8190x_2)} \quad \text{as} \quad |x_2| \to \infty, \tag{6.3}$$

so that they are bounded but do not decay in the far-field (figure 7k), i.e. they are not in the point spectrum. As frequency increases, they move as a complex conjugate pair on predominantly vertical trajectories. Their corresponding modes decay in the far-field (e.g. figure 7n), so they are Rayleigh–Bloch waves.

The two eigenvalue pairs that swap onto the sheet with $I = \varnothing$ just below $k = 4\pi$ (blue curves) previously occupy a series of sheets with $I \neq \varnothing$ (figure 7e–g). They swap to the sheet with $I = \varnothing$ through a fourth-order crossing from the sheet with index $I = \{-2, -1, 0, 1\}$ (figure 7g). Thus, all of the bounded plane-wave components when the eigenvalues are on the branch cuts (6.3) are unbounded at frequencies just below this point (e.g. figure 7m). At even lower frequencies, they occupy the sheets with index sets $I = \{1\}$ and $I = \{2\}$ (figure 7e,f), and result from merging of two pairs of eigenvalues on independent trajectories (blue and cyan curves).

(b) Dispersion curves

The eigenvalue trajectories for the grating of intermediate scatterers ($a = 0.25$) are summarized in dispersion curves (figure 8). The dispersion curves include the Rayleigh–Bloch wavenumbers (eigenvalues in the first Brillouin zone on the sheet with $I = \varnothing$; solid curves) and their extensions/connections on the other sheets (broken curves). The intricate behaviour of the dispersion curves over a short frequency interval just above the Neumann trapped mode frequency is highlighted (zoom-ins). It involves the Rayleigh–Bloch waves transitioning to bandgap behaviour ($\beta \in \mathbb{R}$ to $\beta = \pi \pm \beta_i$; red curves), the cut-on of a second pair of Rayleigh–Bloch wavenumbers (green curves), the subsequent collisions of the Rayleigh–Bloch wavenumber pairs and locking of their trajectories (overlapping of the curves). Further, the dispersion curves emphasize that once the Rayleigh–Bloch wavenumbers (solid red curves) cut off at the Dirichlet trapped mode (eigenvalues swap to a sheet with $I \neq \varnothing$), they do not cut on again in the frequency range considered. Instead, an independent pair of Rayleigh–Bloch waves cut on towards the high-frequency end of the considered range (solid blue curves).
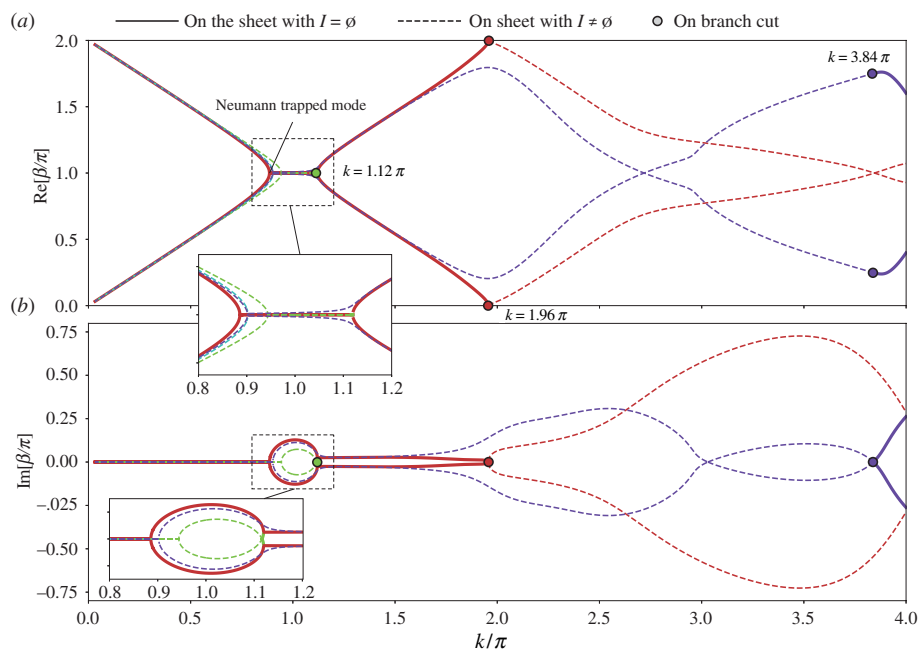
Figure 8. Rayleigh–Bloch wave dispersion curves (eigenvalues on the sheet with $I = \varnothing$) for $a = 0.25$, including extensions onto other sheets. Dispersion curves are for both rightwards and leftwards propagating/decaying modes. Zoom-ins show a pair of Rayleigh–Bloch wavenumbers cutting on above the Neumann trapped mode frequency (green curves) and subsequently interacting with the existing Rayleigh–Bloch wavenumbers on the sheet with $I = \varnothing$ (red curves). Colours are consistent with those in figure 7.

The Rayleigh–Bloch dispersion curves for the grating of small scatterers ($a = 0.15$; figure 9) have similar qualitative properties to those of the grating of intermediate scatterers up to the frequency they cut off at the Dirichlet trapped mode. In this case, two pairs of locked Rayleigh–Bloch waves (overlapping dispersion curves) cut on below $k = 3\pi$ (at $k = 2.55\pi$; solid cyan curves). They exhibit behaviour resembling a passband to bandgap transition as frequency increases, in which pairs of wavenumbers with small imaginary parts meet at $\beta = \pi \pm i\epsilon$ when $k \approx 2.95\pi$. The Rayleigh–Bloch wavenumbers then unlock into two complex conjugate pairs with fixed real parts and varying imaginary parts (see zoom-in). One pair move towards one another (purple curves) and cut off after a very short frequency interval when they meet at $\beta = \pi$. The other pair (cyan curves) veer away from one another before moving back towards one another and cut off when they meet at $\beta = \pi$ for $k \approx 3.15\pi$. No further Rayleigh–Bloch wavenumbers appear up to $k = 4\pi$.

The Rayleigh–Bloch dispersion curves for the grating of large scatterers ($a = 0.35$; figure 10) have different qualitative properties above the Neumann trapped mode frequency to those of the gratings of smaller scatterers. Similar to the gratings of smaller scatterers, an additional pair of Rayleigh–Bloch wavenumbers cut on above the Neumann trapped mode frequency (at $k = 1.22\pi$), collide with the existing pair of Rayleigh–Bloch wavenumbers and then the pairs become locked (left-hand zoom-ins). However, in contrast to the gratings of smaller scatterers, the locked trajectories only last for a short frequency interval before colliding again and unlock back into two complex conjugate pairs. One pair of Rayleigh–Bloch wavenumbers move towards one another and cut off after a short frequency interval (at $k = 1.46\pi$) when they meet at $\beta = \pi$. The other pair veer away from one another up to just above $k = 3\pi$, such that their imaginary parts have large moduli (Im$[\beta]$ up to approx. 2π). Two other pairs of Rayleigh–Bloch wavenumbers cut on just below $k = 3\pi$ (at $k = 2.79\pi$; initially purple curves in right-hand zoom-ins) and follow similar qualitative behaviour to those of the grating of small
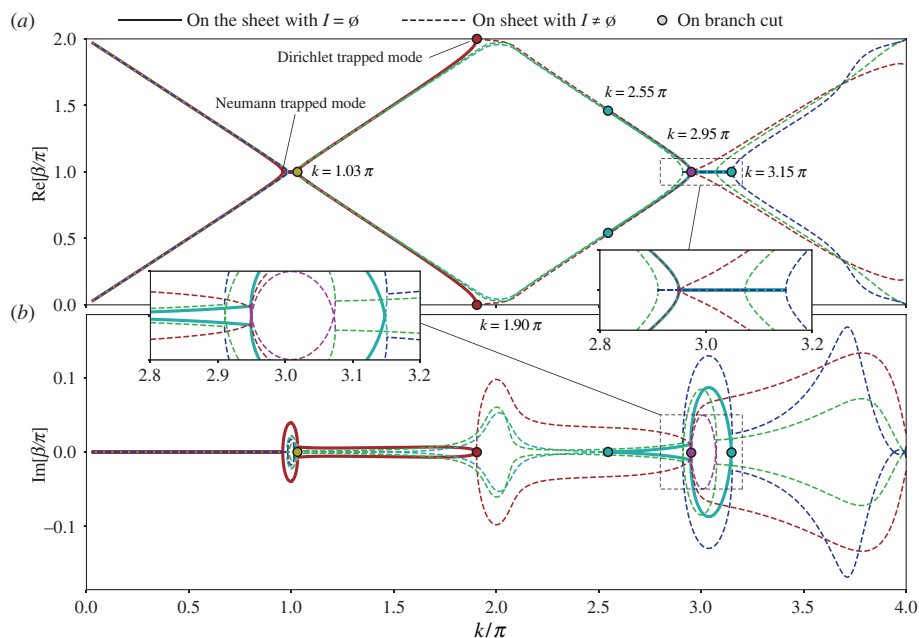
Figure 9. As in figure 8 but for $a = 0.15$. The zoom-in shows behaviour similar to a passband to bandgap transition around $k = 3\pi$.

scatters around $k = 3\pi$, except that the pair that veer away from one another after the two pairs unlock (green curves) collide with the extensions of the classical Rayleigh–Bloch waves (red curves), become locked with them and shortly after cut off at $\beta = 0.106\pi$ and 1.89π for $k = 3.36\pi$. No further Rayleigh–Bloch wavenumbers cut on up to $k = 4\pi$.

7. Concluding remarks

We have presented a Green's function approach to calculate Rayleigh–Bloch waves along gratings of sound-hard scatterers in an acoustic medium, as an alternative to the transfer operator approach of Bennetts and Peter [17]. The Green's function approach formulates the Rayleigh–Bloch modes as non-trivial solutions of a boundary integral equation, which is more challenging than solving the linear eigenvalue problem in [17]. However, it allows the point spectrum to be calculated separately from the continuous spectrum, which facilitates analysis of critical points where Rayleigh–Bloch waves cut on or cut off. The Green's function solution method also gives a convenient ansatz for the far-field of the eigenmodes, which allows the modes to be identified as decaying away from the grating (thus, in the point spectrum, and embedded if the eigenvalue lies on a branch cut) or bounded but non-decaying (thus, in the continuous spectrum). Moreover, the Green's function approach allowed the eigenpairs to be generalized to unbounded solutions that grow away from the array, which allowed Rayleigh–Bloch waves to be tracked in frequency space after they cut off or before they cut on.

The results presented for the Rayleigh–Bloch dispersion curves are largely consistent with those of [17]. The results for the gratings of small and intermediate scatters differ mainly in the short frequency intervals between the Dirichlet trapped mode and $k = 2\pi$. Bennetts and Peter [17] used results with a small artificial damping in the scatterers to argue the Rayleigh–Bloch wavenumbers are embedded in the continuous spectrum over these intervals. In contrast, our results indicate they swap between multiple Riemann sheets. It is possible that the damping could move the eigenvalues back onto the original sheet and, thus, explain the findings in [17].
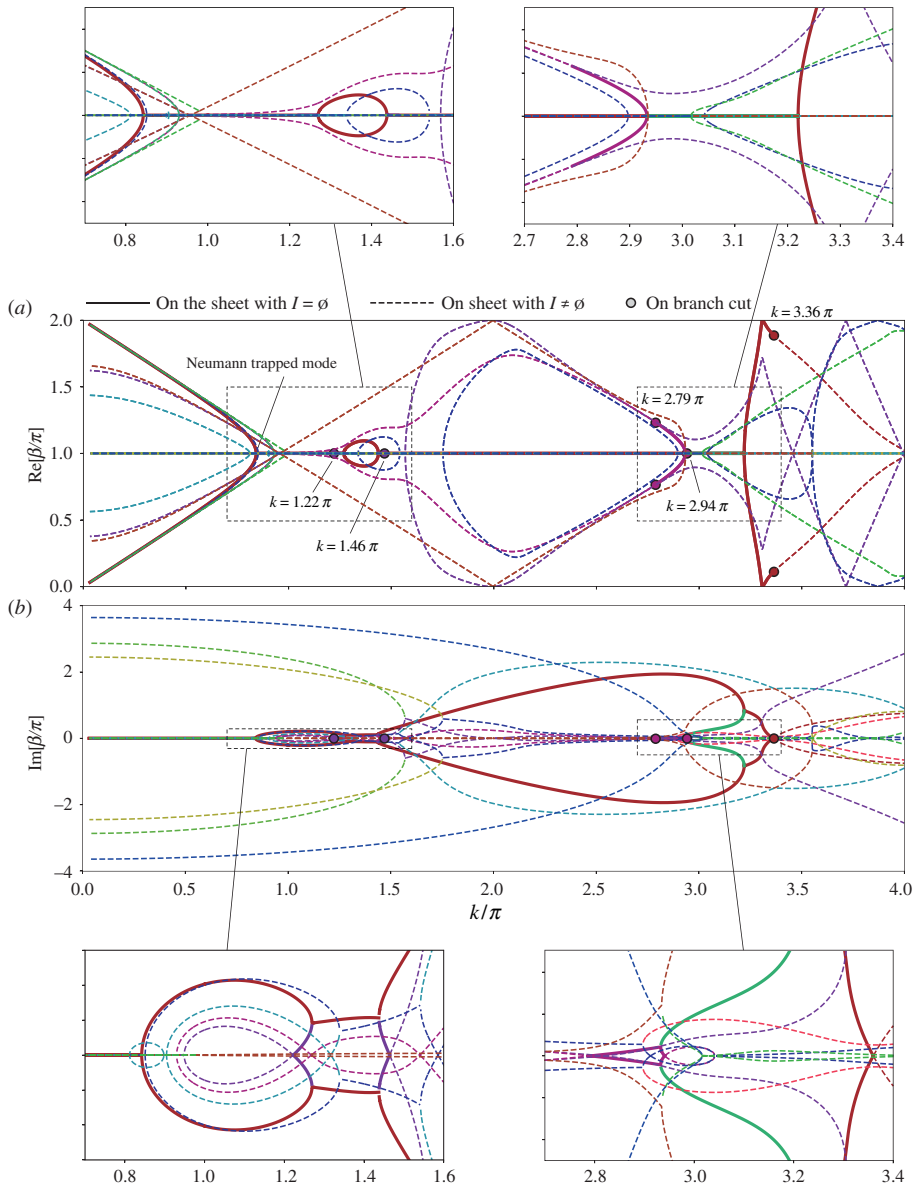
Figure 10. As in figure 8 but for $a = 0.35$. The left-hand zoom-ins show the contrasting behaviour of the Rayleigh–Bloch waves above the Neumann trapped mode frequency to those of the gratings of smaller scatterers (figures 8 and 9). The right-hand zoom-ins show interactions between three pairs of Rayleigh–Bloch wavenumbers around $k = 3\pi$.

The present results better resolve the behaviours of the Rayleigh–Bloch wavenumbers that were obscured by the continuous spectrum in [17], such as the cut-off of one pair of Rayleigh–Bloch wavenumbers above the Neumann trapped mode frequency for the grating of large cylinders and the persistence of the other pair to much higher frequencies. Moreover, the results extend beyond the upper frequency limit of $k = 3\pi$ in [17], for which the results of the transfer operator approach become unstable.

The Green's function approach and tracking algorithm can be extended in a straightforward manner to study Rayleigh–Bloch waves in more general settings, such as with non-circular and non-sound-hard scatterers. (The Green's function is independent of boundary conditions

on the surface of scatterers, and the boundary integral formulation for other linear boundary conditions is well established.) For instance, they may be used to explain the non-existence of classical Rayleigh–Bloch waves for sound-soft scatterers, which is previously reported by Bonnet-Bendhia & Starling [23] based on another mathematical theory. Another future direction is the analysis of Rayleigh–Bloch waves in three dimensions [24], i.e. Bloch waves supported by a singly or doubly periodic array. We expect that the proposed Green's function approach works also for such problems.

Appendix A. Kummer transformation for quasi-periodic Green's function

The Poisson summation form (4.1) is not always suitable for the numerical evaluation of the quasi-periodic Green's function, G_β, since it converges slowly when $x_2 - y_2 = 0$. Another disadvantage is that the logarithmic singularity is not explicit in (4.1). A Kummer transformation is applied [21,26,27], as summarized below.

Let $q_1, \ldots, q_M$ be arbitrary constants with $(\text{Im}[\beta])^2/(kL)^2 < q_1 < q_2 < \cdots < q_M$. The Poisson summation formula gives the identity

$$\frac{1}{2\pi} \sum_{n=-\infty}^{\infty} K_0(\sqrt{q_s}k|\mathbf{x} - \mathbf{y} - n\mathbf{e}_1|)e^{in\beta}$$

$$= \sum_{m=-\infty}^{\infty} \frac{1}{2\sqrt{k_m^2 + q_s k^2}} \exp\left(ik_m(x_1 - y_1)\right) \exp\left(-\sqrt{k_m^2 + q_s k^2}|x_2 - y_2|\right), \quad \text{(A 1)}$$

where K_n is the modified Bessel function of the second kind and order n. Using (A 1), the quasi-periodic Green's function (4.1) can be rewritten as

$$G_\beta(\mathbf{x}, \mathbf{y}; I) = -\frac{1}{2\pi} \sum_{s=1}^{M} c_s \sum_{n=-\infty}^{\infty} K_0(\sqrt{q_s}k|\mathbf{x} - \mathbf{y} - n\mathbf{e}_1|)e^{in\beta}$$

$$+ \sum_{m \in I} \exp\left(ik_m(x_1 - y_1)\right)\left(\frac{-\exp\left(\sqrt{k_m^2 - k^2}|x_2 - y_2|\right)}{2\sqrt{k_m^2 - k^2}} + \sum_{s=1}^{M} c_s \frac{\exp\left(-\sqrt{k_m^2 + q_s k^2}|x_2 - y_2|\right)}{2\sqrt{k_m^2 + q_s k^2}}\right)$$

$$+ \sum_{m \notin I} \exp\left(ik_m(x_1 - y_1)\right)\left(\frac{\exp\left(-\sqrt{k_m^2 - k^2}|x_2 - y_2|\right)}{2\sqrt{k_m^2 - k^2}} + \sum_{s=1}^{M} c_s \frac{\exp\left(-\sqrt{k_m^2 + q_s k^2}|x_2 - y_2|\right)}{2\sqrt{k_m^2 + q_s k^2}}\right), \quad \text{(A 2)}$$

where $c_1, \ldots, c_M \in \mathbb{C}$ are arbitrary. The series converges at the rate of $O(|m|^{-2M-1}e^{-|x_2-y_2|m})$ if the constants $c_1, \ldots, c_M$ are given by

$$c_s = -\prod_{i \neq s} \frac{q_i + 1}{q_i - q_s}. \quad \text{(A 3)}$$

See [21,26,27] for details.

Appendix B. Discretization of the boundary integral equation

The Kress collocation method [28] is used to discretize the hyper-singular boundary integral equation (2.18). The underlying idea is to split the quasi-periodic Green's function into the fundamental solutions with logarithmic singularity and some regular terms. To circumvent the evaluation of the hyper-singular kernel in the boundary integral equation (2.18), the boundary integral equation is rewritten as

$$
2\frac{\partial}{\partial \nu(\mathbf{x})} \int_{\partial \Omega} \frac{\partial G_\beta}{\partial \nu(\mathbf{y})}(x,y;I)\varphi(\mathbf{y})\mathrm{d}s(\mathbf{y})
$$

$$
= 2\frac{\partial}{\partial s(\mathbf{x})} \int_{\partial \Omega} G_\beta(\mathbf{x},\mathbf{y};I)\frac{\partial \varphi}{\partial s}(\mathbf{y})\mathrm{d}s(\mathbf{y}) + 2k^2 \nu(\mathbf{x}) \cdot \int_{\partial \Omega} G_\beta(\mathbf{x},\mathbf{y};I)\nu(\mathbf{y})\varphi(\mathbf{y})\mathrm{d}s(\mathbf{y}),
\tag{B 1}
$$

provided that the density φ is Hölder continuous [28], where $\frac{\partial}{\partial s}$ denotes the tangential derivative. Using this identity, the boundary integral equation (2.18) is reformulated as

$$
2\frac{\partial}{\partial s(\mathbf{x})} \int_{\partial \Omega} G_\beta(\mathbf{x},\mathbf{y};I)\frac{\partial \varphi}{\partial s}(\mathbf{y})\mathrm{d}s(\mathbf{y}) + 2k^2 \nu(\mathbf{x}) \cdot \int_{\partial \Omega} G_\beta(\mathbf{x},\mathbf{y};I)\nu(\mathbf{y})\varphi(\mathbf{y})\mathrm{d}s(\mathbf{y})
$$

$$
-2i\eta \int_{\partial \Omega} \frac{\partial G_\beta}{\partial \nu(\mathbf{x})}(\mathbf{x},\mathbf{y};I)\varphi(\mathbf{y})\mathrm{d}s(\mathbf{y}) + i\eta \varphi(\mathbf{x}) = 0.
\tag{B 2}
$$

Assume that Ω is connected and its boundary $\partial \Omega$ is sufficiently smooth, such that there exist 2π-periodic functions $x_1(t)$ and $x_2(t)$ of class C^3, such that

$$
\partial \Omega = \{(x_1(t), x_2(t)) : t \in [0,2\pi]\},
\tag{B 3}
$$

with $|x_1'(t)| > 0$ and $|x_2'(t)| > 0$ for all $t \in [0,2\pi]$. Without loss of generality, the parametrization is assumed to be counter-clockwise, so that the unit outward normal vector at $\mathbf{x}(t)$ is given by $\boldsymbol{\nu}(t) := (x_2'(t), -x_1'(t))^T/|\mathbf{x}'(t)|$. The boundary parametrization converts the first term on the left-hand side of (B 2) as

$$
2\frac{\partial}{\partial s(\mathbf{x})} \int_{\partial \Omega} G_\beta(\mathbf{x},\mathbf{y};I)\frac{\partial \varphi}{\partial s}(\mathbf{y})\mathrm{d}s(\mathbf{y}) = \frac{2}{|\mathbf{x}'(t)|} \int_0^{2\pi} \frac{\partial}{\partial t} G_\beta(\mathbf{x}(t), \mathbf{x}(\tau);I)\psi'(\tau)\mathrm{d}\tau,
\tag{B 4}
$$

where the 2π-periodic density ψ is defined by $\psi(t) = \varphi(x(t))$. The quasi-periodic Green's function (kernel) is split into singular and regular terms as

$$
G_\beta(\mathbf{x},\mathbf{y};I) = -\frac{1}{2\pi} \sum_{s=1}^M c_s K_0(\sqrt{q_s}k|\mathbf{x}-\mathbf{y}|) + G_\beta^R(\mathbf{x},\mathbf{y};I),
\tag{B 5}
$$

where $G_\beta^R(\mathbf{x},\mathbf{y};I)$ is continuous at $\mathbf{x} = \mathbf{y}$. Using (B 5) and integration by parts, the right-hand side of (B 4) is rewritten as

$$
\frac{2}{|\mathbf{x}'(t)|} \int_0^{2\pi} \frac{\partial}{\partial t} G_\beta(\mathbf{x}(t), \mathbf{x}(\tau);I)\psi'(\tau)\mathrm{d}\tau
$$

$$
= \frac{-1}{2\pi} \frac{1}{|\mathbf{x}'(t)|} \int_0^{2\pi} \cot\frac{t-\tau}{2}\psi'(\tau)\mathrm{d}\tau
$$

$$
+ \frac{1}{|\mathbf{x}'(t)|} \int_0^{2\pi} \left[\sum_{s=1}^M c_s \frac{\partial^2}{\partial t \partial \tau} \left(\frac{1}{\pi} K_0(\sqrt{q_s}k|\mathbf{x}(t)-\mathbf{x}(\tau)|) + \frac{1}{2\pi}\log\left(4\sin^2\frac{t-\tau}{2}\right) \right) \right.
$$

$$
\left. - 2\frac{\partial^2}{\partial t \partial \tau} G_\beta^R(\mathbf{x}(t), \mathbf{x}(\tau);I) \right] \psi(\tau)\mathrm{d}\tau,
\tag{B 6}
$$

where we have used

Table 1. Convergence of Rayleigh–Bloch wavenumber for circular scatterers of radius $a = 0.25$, on the sheet with $I = \varnothing$ at frequency $k = \pi$, with respect to N and M.

N	$\mathrm{Re}[\beta/\pi]$		$\mathrm{Im}[\beta/\pi]$	
	$M = 3$	$M = 5$	$M = 3$	$M = 5$
4	0.999962254743528	0.999955076952821	0.127504679308788	0.127510731339907
8	1.000000080009148	0.999955076952821	0.127392775182671	0.127392827042699
12	1.000000010154917	0.999999999999999	0.127392816799418	0.127392823262497
16	1.000000002365567	0.999999999999999	0.127392821757663	0.127392823262422
20	1.000000000768575	0.999999999999996	0.127392822773655	0.127392823262426
24	1.000000000307452	0.999999999999984	0.127392823066931	0.127392823262433
28	1.000000000141854	1.000000000000012	0.127392823172234	0.127392823262413
32	1.000000000072627	0.999999999999976	0.127392823216250	0.127392823262438
36	1.000000000040253	1.000000000000002	0.127392823236833	0.127392823262419
40	1.000000000023747	0.999999999999995	0.127392823247326	0.127392823262424

$$\sum_{s=1}^{M} c_s = -1. \tag{B 7}$$

Note that the kernel in the second term on the right-hand side of (B 6) is also continuous. The second and third terms on the left-hand side of (B 2) can be treated in an analogous manner. After some straightforward calculations, we obtain the integral equation

$$-\frac{1}{2\pi}\int_0^{2\pi} \cot\frac{t-\tau}{2}\psi'(\tau)\mathrm{d}\tau + \int_0^{2\pi} K_\beta(t,\tau;I)\psi(\tau)\mathrm{d}\tau + i\eta|\mathbf{x}'(t)|\psi(t) = 0, \tag{B 8}$$

which is equivalent to (B 2). The kernel K_β is defined by

$$K_\beta(t,\tau;I) = \sum_{s=1}^{M} c_s \frac{\partial^2}{\partial t \partial \tau}\left[\frac{1}{\pi}K_0(\sqrt{q_s}k\,|\mathbf{x}(t)-\mathbf{x}(\tau)|) + \frac{1}{2\pi}\log\left(4\sin^2\frac{t-\tau}{2}\right)\right]$$
$$- 2\frac{\partial^2}{\partial t \partial \tau}G_\beta^R(\mathbf{x}(t),\mathbf{x}(\tau);I) + 2k^2 G_\beta(\mathbf{x}(t),\mathbf{x}(\tau);I)\nu(t)\cdot\nu(\tau)|\mathbf{x}'(t)|\,|\mathbf{x}'(\tau)|$$
$$- 2i\eta\nu(t)\cdot\nabla_x G_\beta(\mathbf{x},\mathbf{x}(\tau);I)|_{\mathbf{x}=\mathbf{x}(t)}\,|\mathbf{x}'(t)|\,|\mathbf{x}'(\tau)|\,. \tag{B 9}$$

For the numerical quadrature of the boundary integral (B 8), the kernel K_β is split into two terms as

$$K_\beta(t,\tau;I) = K_\beta^1(t,\tau)\log\left(4\sin^2\frac{t-\tau}{2}\right) + K_\beta^2(t,\tau;I), \tag{B 10}$$

$$K_\beta^1(t,\tau) := \frac{k^2}{2\pi}\nu(t)\cdot\nu(\tau)|\mathbf{x}'(t)|\,|\mathbf{x}'(\tau)|\sum_{s=1}^{M}c_s I_0(\sqrt{q_s}k\,|\mathbf{x}(t)-\mathbf{x}(\tau)|)$$
$$- \frac{ik\eta}{2\pi}\frac{\nu(t)\cdot(\mathbf{x}(t)-\mathbf{x}(\tau))}{|\mathbf{x}(t)-\mathbf{x}(\tau)|}|\mathbf{x}'(t)|\,|\mathbf{x}'(\tau)|\sum_{s=1}^{M}c_s\sqrt{q_s}I_1(\sqrt{q_s}k\,|\mathbf{x}(t)-\mathbf{x}(\tau)|)$$
$$+ \frac{k}{2\pi}\sum_{s=1}^{M}c_s\sqrt{q_s}\left[\sqrt{q_s}k I_0(\sqrt{q_s}k\,|\mathbf{x}(t)-\mathbf{x}(\tau)|)\zeta(t,\tau)\right.$$
$$\left. + \frac{I_1(\sqrt{q_s}k\,|\mathbf{x}(t)-\mathbf{x}(\tau)|)}{|\mathbf{x}(t)-\mathbf{x}(\tau)|}(\mathbf{x}'(t)\cdot\mathbf{x}'(\tau) - 2\zeta(t,\tau))\right], \tag{B 11}$$

where ζ is defined by

$$\zeta(t,\tau) := \frac{[\mathbf{x}'(t)\cdot(\mathbf{x}(t)-\mathbf{x}(\tau))][\mathbf{x}'(\tau)\cdot(\mathbf{x}(t)-\mathbf{x}(\tau))]}{|\mathbf{x}(t)-\mathbf{x}(\tau)|^2}, \tag{B 12}$$

and I_n is the modified Bessel function of the first kind and order n. Note that the kernel K_β^1 is analytic while $K_\beta^2(\cdot,\cdot;I)$ is only of class C^k for some positive integer k due to the function G_β^R. The differentiability of $K_\beta^2(\cdot,\cdot;I)$ is improved as the parameter M increases. The split of the kernel K_β gives the integral equation

$$-\frac{1}{2\pi}\int_0^{2\pi}\cot\frac{t-\tau}{2}\psi'(\tau)\mathrm{d}\tau + \int_0^{2\pi}K_\beta^1(t,\tau;I)\log\!\Big(4\sin^2\frac{t-\tau}{2}\Big)\psi(\tau)\mathrm{d}\tau$$
$$+\int_0^{2\pi}K_\beta^2(t,\tau;I)\psi(\tau)\mathrm{d}\tau + \mathrm{i}\eta\,|\mathbf{x}'(t)|\,\psi(t) = 0, \tag{B 13}$$

equivalent to (B 8). Approximate solutions of (B 13) are sought in a $2N$-dimensional space of trigonometric functions with sufficiently large integer N. First, substitute the expansion

$$\psi(t) \simeq \sum_{j=0}^{2N-1}\Psi_j L_j(t) \tag{B 14}$$

with unknown coefficients $\Psi_j \in \mathbb{C}$ into (B 13) and then collocate the equation at $t = t_j := j\pi/N$ for $j = 0,\ldots,2N-1$, where the functions L_j are defined by

$$L_j(t) = \frac{1}{2N}\Bigg[1 + \cos N(t-t_j) + 2\sum_{l=1}^{N-1}\cos l(t-t_j)\Bigg]. \tag{B 15}$$

The quadrature rules in [28] generate the linear system

$$\sum_{j=0}^{2N-1}\mathcal{A}_{ij}(k,\beta;I)\Psi_j = 0 \tag{B 16}$$

with coefficient matrix

$$\mathcal{A}_{ij}(k,\beta;I) := T_{|i-j|} + R_{|i-j|}K_\beta^1(t_i,t_j) + \frac{\pi}{n}K_\beta^2(t_i,t_j;I) + \mathrm{i}\eta\,|\mathbf{x}'(t_i)|\,\delta_{ij}, \tag{B 17}$$

where the constants R_l and T_l are defined by

$$R_l := -\frac{(-1)^l\pi}{N^2} - \frac{2\pi}{N}\sum_{m=1}^{N-1}\frac{1}{m}\cos\frac{ml\pi}{N}, \tag{B 18}$$

$$T_l := \begin{cases} -\dfrac{N}{2} & l = 0, \\[2mm] \dfrac{1}{2N\sin^2(t_l/2)} & l \text{ is odd}, \\[2mm] 0 & \text{otherwise}. \end{cases} \tag{B 19}$$

Unlike the original scheme [28], spectral accuracy is not possible in terms of N, even if the boundary is of class C^∞, due to the lack of the analyticity of the kernel K_β^2. Thus, exponential convergence of the trapezoidal rule is not available. Nevertheless, the convergence of the trapezoidal rule becomes faster as the parameter M is increased. This implies that the parameter M controls the accuracy of the proposed scheme.

Consider circular scatterers with radius $a = 0.25$, and frequency $k = \pi$. The block SSM (§5a) applied on the boundary integral equation finds a single Rayleigh–Bloch wavenumber (eigenvalue) in the first irreducible Brillouin zone of the physical sheet (table 1), using a circular path of radius 0.02 centred at $\beta = \pi + 0.4\mathrm{i}$ in the complex β-plane, and by dividing the path into 40 segments for the trapezoidal rule. As the parameter N is increased, the values converge to $\beta/\pi = 1 + 0.127392823\mathrm{i}$. This convergence is faster in the case of $M = 5$ than in the case of $M = 3$ due to the singular-part split of the quasi-periodic Green function. The Rayleigh–Bloch

wavenumber computed is consistent with the value $\beta/\pi \approx 1 + 0.127i$ previously reported by Bennetts and Peter [17].

References

1. Linton CM, McIver M. 2002 The existence of Rayleigh–Bloch surface waves. *J. Fluid Mech.* **470**, 85–90. (doi:10.1017/S0022112002002227)
2. Porter R, Evans DV. 1999 Rayleigh–Bloch surface waves along periodic gratings and their connection with trapped modes in waveguides. *J. Fluid Mech.* **386**, 233–258. (doi:10.1017/S0022112099004425)
3. Brekhovskikh L. 1959 Surface waves in acoustics. *Sov. Phys. Acoust.* **5**, 3. (doi:10.1070/PU1960v003n01ABEH003263)
4. Peter MA, Meylan MH. 2007 Water-wave scattering by a semi-infinite periodic array of arbitrary bodies. *J. Fluid Mech.* **575**, 473–494. (doi:10.1017/S0022112006004319)
5. Colquitt DJ, Craster RV, Antonakakis T, Guenneau S. 2015 Rayleigh–Bloch waves along elastic diffraction gratings. *Proc. R. Soc. A* **471**, 20140465. (doi:10.1098/rspa.2014.0465)
6. Chaplain GJ, Makwana MP, Craster RV. 2019 Rayleigh–Bloch, topological edge and interface waves for structured elastic plates. *Wave Motion* **86**, 162–174. (doi:10.1016/j.wavemoti.2019.01.008)
7. Linton CM, McIver P. 2007 Embedded trapped modes in water waves and acoustics. *Wave Motion* **45**, 16–29. (doi:10.1016/j.wavemoti.2007.04.009)
8. Maniar HD, Newman JN. 1997 Wave diffraction by a long array of cylinders. *J. Fluid Mech.* **339**, 309–330. (doi:10.1017/S0022112097005296)
9. Linton CM, Porter R, Thompson I. 2007 Scattering by a semi-infinite periodic array and the excitation of surface waves. *SIAM J. Appl. Math.* **67**, 1233–1258. (doi:10.1137/060672662)
10. Thompson I, Linton CM, Porter R. 2008 A new approximation method for scattering by long finite arrays. *Q. J. Mech. Appl. Math.* **61**, 333–352. (doi:10.1093/qjmam/hbn006)
11. Bennetts LG, Peter MA, Montiel F. 2017 Localisation of Rayleigh–Bloch waves and damping of resonant loads on arrays of vertical cylinders. *J. Fluid Mech.* **813**, 508–527. (doi:10.1017/jfm.2016.855)
12. Bennetts LG, Peter MA, Craster RV. 2018 Graded resonator arrays for spatial frequency separation and amplification of water waves. *J. Fluid Mech.* **854**. (doi:10.1017/jfm.2018.648)
13. Archer AJ, Wolgamot HA, Orszaghova J, Bennetts LG, Peter MA, Craster RV. 2020 Experimental realization of broadband control of water-wave-energy amplification in chirped arrays. *Phys. Rev. Fluids* **5**, 062801. (doi:10.1103/PhysRevFluids.5.062801)
14. McIver P. 2000 Water-wave propagation through an infinite array of cylindrical structures. *J. Fluid Mech.* **424**, 101–125. (doi:10.1017/S0022112000001774)
15. Bennetts LG, Peter MA, Craster RV. 2019 Low-frequency wave-energy amplification in graded two-dimensional resonator arrays. *Phil. Trans. R. Soc. A* **377**, 20190104. (doi:10.1098/rsta.2019.0104)
16. Porter R, Evans DV. 2005 Embedded Rayleigh–Bloch surface waves along periodic rectangular arrays. *Wave Motion* **43**, 29–50. (doi:10.1016/j.wavemoti.2005.05.005)
17. Bennetts LG, Peter MA. 2022 Rayleigh–Bloch waves above the cutoff. *J. Fluid Mech.* **940**, A35. (doi:10.1017/jfm.2022.247)
18. Chaplain GJ, Hawkins SC, Peter MA, Bennetts LG, Starkey TA. 2024 Acoustic lattice resonances and generalised Rayleigh–Bloch waves. *arXiv.* (doi:10.48550/arXiv.2409.10074)
19. Twersky V. 1962 On scattering of waves by the infinite grating of circular cylinders. *IRE Trans. Antennas Propag.* **10**, 737–765. (doi:10.1109/TAP.1962.1137940)
20. Peter MA, Meylan MH, Linton CM. 2006 Water-wave scattering by a periodic array of arbitrary bodies. *J. Fluid Mech.* **548**, 237. (doi:10.1017/S0022112005006981)
21. Linton CM. 1998 The Green's function for the two-dimensional Helmholtz equation in periodic domains. *J. Eng. Math.* **33**, 377–401. (doi:10.1023/A:1004377501747)

24

royalsocietypublishing.org/journal/rspa *Proc. R. Soc. A* **480:** 20240211

22. Asakura J, Sakurai T, Tadano H, Ikegami T, Kimura K. 2009 A numerical method for nonlinear eigenvalue problems using contour integrals. *JSIAM Let.* **1**, 52–55. (doi:10.14495/jsiaml.1.52)

23. Bonnet-Bendhia A, Starling F. 1994 Guided waves by electromagnetic gratings and non-uniqueness examples for the diffraction problem. *Math. Methods Appl. Sci.* **17**, 305–338. (doi:10.1002/mma.1670170502)

24. Thompson I, Linton CM. 2010 Guided surface waves on one- and two-dimensional arrays of spheres. *SIAM J. Appl. Math.* **70**, 2975–2995. (doi:10.1137/100787519)

25. Matsushima K. 2024 Rayleigh-Bloch-Green. *Zenodo.* (doi:10.5281/zenodo.10846715)

26. Bennetts LG, Squire VA. 2010 Linear wave forcing of an array of axisymmetric ice floes. *IMA J. Appl. Math.* **75**, 108–138. (doi:10.1093/imamat/hxp038)

27. Matsushima K, Isakari H, Takahashi T, Matsumoto T. 2021 A topology optimisation of composite elastic metamaterial slabs based on the manipulation of far-field behaviours. *Struct. Multidiscipl. Optim.* **63**, 231–243. (doi:10.1007/s00158-020-02689-y)

28. Kress R. 1995 On the numerical solution of a hypersingular integral equation in scattering theory. *J. Comput. Appl. Math.* **61**, 345–360. (doi:10.1016/0377-0427(94)00073-7)